

The Thermodynamic Cycles and Associated Energetics of Hurricane Edouard (2014) during Its Intensification

JUAN FANG

Key Laboratory for Mesoscale Severe Weather, Ministry of Education, and School of Atmospheric Science, Nanjing University, Nanjing, China

OLIVIER PAULUIS

Courant Institute for Applied Mathematics, New York University, New York, New York

FUQING ZHANG

Department of Meteorology and Atmospheric Sciences, and Center for Advanced Data Assimilation and Predictability Techniques, The Pennsylvania State University, University Park, Pennsylvania

(Manuscript received 31 July 2018, in final form 2 April 2019)

ABSTRACT

This study expands on a previous analysis of the intensification of Hurricane Edouard (2014) in the isentropic coordinates to further examine the thermodynamic processes that lead to the strengthening of the storm. Thermodynamic cycles are extracted using the methodology known as the Mean Airflow as Lagrangian Dynamics Approximation. The most intense thermodynamic cycle here is associated with the air rising within the hurricane eyewall. Its structure remains mostly steady during the early development of Edouard but evolves rapidly as the storm intensifies. Through intensification, the ascent shifts toward high values of entropy under the effect of enhanced surface heat fluxes and stronger surface winds, while reaching higher altitudes and lower temperatures. The near-rapid intensification onset of Edouard corresponds to an increase in the energy input into the cycle and an increase in the amount of kinetic energy generated. The external heating fluctuates considerably in the two low-level legs with a period of about 16–24 h, indicative of diurnal variation in the thermodynamic cycle. During the intensification of Edouard, the mechanical work production and the Carnot efficiency both increase dramatically, which can be attributed to the increase in energy transport and deepening of the thermodynamic cycle. In addition, there is a substantial increase of the mechanical work done during the horizontal expansion of air parcels near Earth's surface, and a larger fraction of the kinetic energy generated is used to sustain and intensify the horizontal flow rather than to provide a vertical acceleration in the updrafts.

1. Introduction

A tropical cyclone (TC) is one of the most fascinating atmospheric phenomena, which draws energy from the ocean to strengthen itself. As it becomes intense, it can acquire enormous energy with potentially catastrophic impacts for the population in its path. How a weak tropical disturbance develops into an intense storm is a question of great importance and has been the subject of much research in our field. Early investigators suggested that an incipient tropical disturbance can intensify and ultimately develops into a TC via the positive feedback

process related to the cooperative interaction between deep convection and surface large-scale circulation, which is commonly known as the conditional instability of the second kind (CISK) mechanism (Charney and Eliassen 1964; Ooyama 1964). Later on, the air-sea interaction instability paradigm [what is now commonly known as the wind-induced surface heat exchange (WISHE) mechanism] proposed by Emanuel (1986) and Rotunno and Emanuel (1987) has been considered as the leading hypothesis for TC intensification. Under WISHE, enhanced surface winds increase fluxes of sensible and latent heat from the ocean, and deep moist convection transports the energy from the ocean surface to the upper troposphere. This in turn increases

Corresponding author: Dr. Juan Fang, fangjuan@nju.edu.cn

the temperature at the center of the storm and further strengthens the surface winds. The positive feedback between surface winds and energy exchange fluxes will lead to the TC intensification.

In both CISK and WISHE, the intensification of a TC requires converting internal energy into kinetic energy to strengthen the winds while also countering dissipation arising from surface friction and turbulence in the free atmosphere. To this effect, the TC acts as a kind of heat engine described by [Eliassen and Kleinschmidt \(1957\)](#). [Anthes \(1974\)](#) suggested that a TC is a quasi-steady thermodynamic heat engine driven primarily by latent heat release, in which the release of latent heat in the warm core maintains the TC's baroclinic structure and generates available potential energy, which is continuously converted to kinetic energy. [Emanuel \(1986\)](#) argued that the TC is more of a simple Carnot heat engine that converts heat energy extracted from the ocean to mechanical energy. Such a Carnot cycle is composed of four legs (segments), in which a single air parcel follows a well-defined set of thermodynamic transformations including: spiraling in toward the TC center and gaining entropy from the sea surface at fixed temperature in leg 1, ascending within deep convection in the TC's eyewall and then flowing out to large radius in leg 2, descending slowly in the lower stratosphere with a nearly constant temperature under the effect of radiative cooling in leg 3, and finally descending to the lower troposphere along an absolute angular momentum surface in leg 4.

While viewing TCs as heat engines is a useful analogy that helps us explain storm intensification and maintenance, it is less straightforward to apply this concept to examine energy conversion in a TC quantitatively. The atmosphere, including TCs in particular, is a highly turbulent system. An air parcel's trajectory can vary greatly in space and time and almost never constitutes a perfect closed thermodynamic cycle. Therefore, the TC's thermodynamic cycles are difficult to clearly identify or quantify from observations and numerical simulations. In the thermodynamic cycle proposed by [Emanuel \(1986\)](#), the isothermal descending of the air parcel in leg 3 is derived from the assumption that the upper-level outflow occurs at constant temperature in a TC. However, [Emanuel and Rotunno \(2011\)](#) argued that this assumption is not justified in the TC simulated by a convection-resolving numerical model, in which the upper-level outflow exhibits marked thermal stratification. They proposed that the small-scale turbulence that limits the Richardson number in the TC core sets the stratification of the outflow. In the revised framework, the outflow temperature varies with angular momentum, which also permits the vortex to

intensify with time as that simulated using a full-physics axisymmetric model ([Emanuel and Rotunno 2011](#); [Emanuel 2012](#)). These findings mean that the energy loss in the descending leg of thermodynamic cycle should not be approximately isothermal in the upper levels.

Recently, [Pauluis \(2016\)](#) introduced the Mean Airflow as Lagrangian Dynamics Approximation (MAFALDA), a systematic approach designed to extract a set of representative thermodynamic cycles from numerical simulations of complex atmospheric motions. MAFALDA is based on the isentropic analysis technique in the isentropic framework. By separating the vertical mass transport in terms of equivalent potential temperature θ_e for the rising air parcels at high entropy from the subsiding air at low entropy, the overturning circulation in the θ_e - z space can be computed, which is then used to construct the thermodynamic cycles. With MAFALDA, [Pauluis and Zhang \(2017\)](#) extracted the thermodynamic cycles of a numerically simulated TC from the standard model output. By analyzing the thermodynamic transformations along various representative cycles, they showed that the deepest overturning circulation associated with the rising air within the eyewall is an efficient heat engine that produces about 70% as much kinetic energy as a comparable Carnot cycle.

In our recent study ([Fang et al. 2017](#)), the isentropic analysis technique in the isentropic framework is extended to the convection-permitting simulation of a real-world TC, Hurricane Edouard (2014), with the focus on the changes of the dynamic and thermodynamic structure in the θ_e - z space during the intensification, especially before and after the onset of near-rapid intensification. In the present work, the intensification of Edouard will be further analyzed by examining the thermodynamic cycles extracted with MAFALDA from the model output. The focus of the current study is the variation of the thermodynamic cycles and associated energetics of the storm during its intensification.

The remainder of this paper is organized as follows. [Section 2](#) describes the Edouard simulation and reconstruction of thermodynamic cycles via MAFALDA. [Section 3](#) analyzes the energy gain and loss as well as work production along the cycle associated with the deepest overturning circulation in Edouard. Concluding remarks are given in [section 4](#).

2. Edouard simulation and reconstruction of the thermodynamic cycles via MAFALDA

Edouard formed as a TC at about 1200 UTC 11 September 2014 and developed into the first major

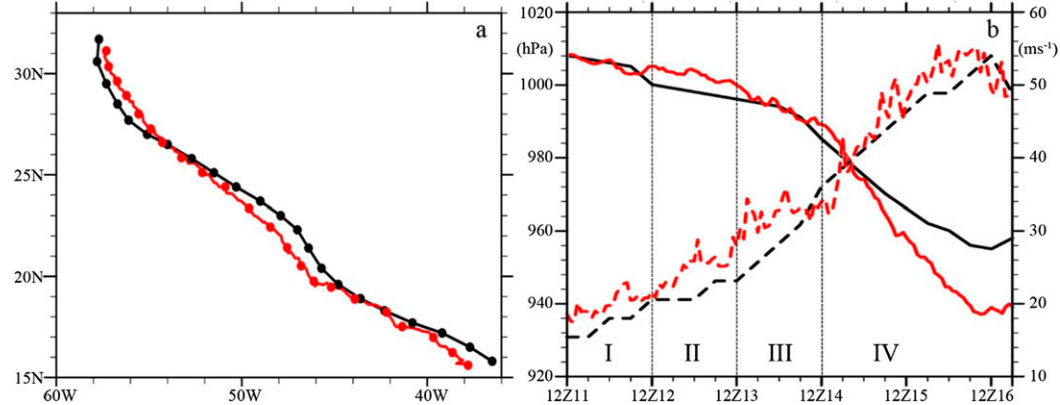


FIG. 1. The NHC best track analysis (black) and model-simulated (red) (a) track and (b) minimum sea level pressure (solid line) and maximum surface wind (dashed line) of Hurricane Edouard. The vertical thin dashed lines denote the onset of stage II, III, and IV from the left to the right, respectively.

hurricane in the Atlantic since Hurricane Sandy (2012) early on 16 September 2014 (Stewart 2014). Its near-rapid intensification and secondary eyewall formation have drawn the attention of many studies (e.g., Rogers et al. 2016; Tang and Zhang 2016; Fang et al. 2017; Leighton et al. 2018; Melhauser et al. 2017; Munsell et al. 2017, 2018; Tang et al. 2017). In this work, the energetics and thermodynamic behavior of Edouard are to be addressed by applying MAFALDA to the simulation (prediction) of Edouard produced by the Weather Research and Forecasting (WRF) Model, version 3.5.1 (Skamarock and Klemp 2008), which was a real-time forecast generated by the Pennsylvania State University (PSU) real-time Atlantic hurricane forecast and analysis system (Zhang et al. 2009, 2011; Zhang and Weng 2015; Weng and Zhang 2016). The model domain is triply nested through two-way nesting with horizontal resolutions of 27, 9, and 3 km, respectively. Both nested domains move to keep the model TC in the center area of the domains. All three domains have 43 vertical levels with the model top at 10 hPa. The integration is conducted for 126 h beginning at 1200 UTC 11 September 2014. The details of the model physics configuration and initialization processes can be found in Munsell et al. (2015, 2017) and Weng and Zhang (2016). The PSU WRF real-time forecast predicts the track and intensification of the observed storm well on the whole except that 1) the deviation of the modeled track from the observed is comparatively large before 1800 UTC 13 September, 2) the near-rapid intensification occurs about 12 h later than observed, and 3) the predicted Edouard is slightly stronger than that estimated by the best track observation (Fig. 1). The proper prediction of the track and intensity changes implies that the development process of Edouard may have been well

captured by the numerical model, based on which the thermodynamic cycles and energetics of Edouard will be examined via MAFALDA.

Following Pauluis (2016) and Pauluis and Zhang (2017), MAFALDA is applied to the numerical simulation via the following two steps:

- 1) Computing the isentropic streamfunction in θ_e-z coordinates with the formula written as

$$\Psi_{\theta_e}(\theta_e, z, t) = \int_0^{\theta_e} \langle \rho w' \rangle (\theta_{e_0}, z, t) d\theta_{e_0}, \quad (1)$$

where Ψ_{θ_e} is the isentropic streamfunction, ρ the air density, w' the perturbation vertical velocity representing the deviation of vertical velocity from the domain-averaged vertical motion,¹ (θ_{e_0}, z) denotes the spatial position of an air parcel in the isentropic coordinates, and $\langle \cdot \rangle$ represents the variable being sorted by equivalent potential temperature; that is,

$$\langle \rho w' \rangle (\theta_{e_0}, z, t) = \iint_A \rho w \delta\{\theta_{e_0} - \theta_e(x, y, z, t)\} dx dy, \quad (2)$$

where $\delta\{\cdot\}$ is the Dirac delta function. In this work, the vertical mass flux defined in Eq. (2) is

¹ Because of the small simulation domain, the domain-averaged vertical velocity is removed in the vertical mass flux to ensure that the isentropic streamfunction is closed in the thermodynamic space (θ_e-z). The horizontal integral is taken over the domain centered at the storm center with side length of 600 km in the present work. For the current study on the intensification of Edouard, the results are generally not sensitive to this manipulation because the domain-averaged vertical velocity is small ($\ll 0.05 \text{ m s}^{-1}$) during the intensification of Edouard.

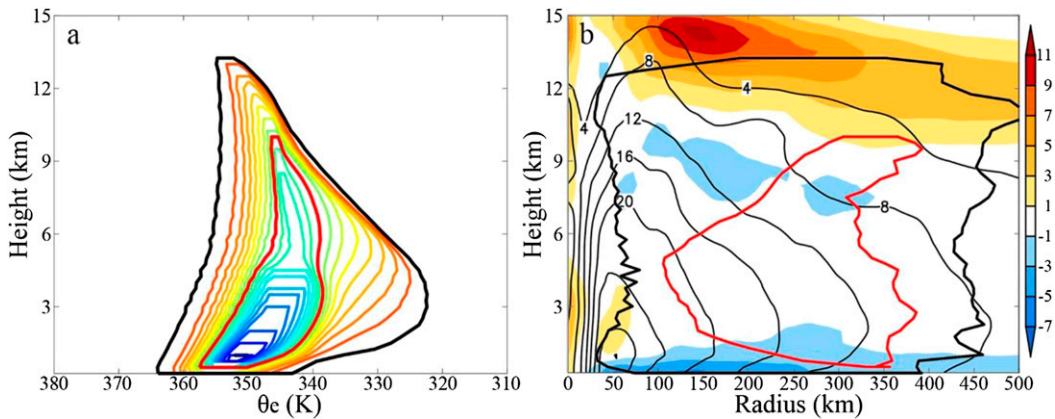


FIG. 2. (a) The isentropic streamfunction and corresponding mean “parcel” trajectories in θ_e – z space at 1200 UTC 14 Sep. The warmer and colder colors denote less and more negative isentropic streamfunction and the trajectories corresponding to smaller and larger values of k in Eq. (3), respectively. The trajectories corresponding to $k = 1$ and $k = 9$ are highlighted by the thick black and thick red curves, respectively. (b) The trajectories corresponding to $k = 1$ (black) and $k = 9$ (red) in the r – z space. The shading denotes the symmetric radial velocity (m s^{-1}), and contours denote the tangential wind (m s^{-1}) at 1200 UTC 14 Sep.

approximated by summing the mass flux over the finite-size θ_e bins; that is, $\theta_{e_0} - 1/8 < \theta_e \leq \theta_{e_0} + 1/8$ K. The isentropic streamfunction derived from Eqs. (1) and (2) at 1200 UTC 14 September when the near-rapid intensification started is shown in Fig. 2a.

According to Pauluis and Mrowiec (2013), the isopleths of the isentropic streamfunction correspond to the mean trajectories in the θ_e – z space in the sense that the vector composed of conditional averaged diabatic tendency and vertical velocity is parallel to the isolines of the isentropic streamfunction in the θ_e – z space. Henceforth, MAFALDA takes the isopleths of the isentropic streamfunction as the mean “parcel” trajectories in the θ_e – z space (Pauluis 2016). By this way, an arbitrary set of trajectories in θ_e – z space can be determined from fractions of the minimum streamfunction. In Fig. 2a, there are 20 isopleths of the isentropic streamfunction with the values of $[(2k - 1)/2N]\min\Psi$, where $1 \leq k \leq N$ and $N = 20$, which are corresponding to 20 distinct trajectories with (θ_{ek}, z_k) satisfying the following equation:

$$\Psi_{\theta_e}(\theta_{ek}, z_k) = \frac{2k - 1}{2N} \min_{\theta_e, z} \Psi, \quad \text{where } 1 \leq k \leq N$$

(3)

and $N = 20$.

By finding (θ_{ek}, z_k) satisfying Eq. (3), the trajectories can be determined, which are shown in Fig. 2a. From Fig. 2a we can see that there are deep and shallow overturning circulations in Edouard. For simplicity, the trajectories corresponding to $k = 1$

and $k = 9$ are subjectively chosen to represent the deepest and shallower overturning circulations in Edouard,² respectively. Figure 2b shows that the ascending branch of the former locates in the eyewall region while the ascending branch of the latter situates in the outer-core area at 1200 UTC 14 September, which is consistent with Pauluis and Zhang (2017).

The MAFALDA trajectories (θ_{ek}, z_k) determined above are cyclical, along which any thermodynamic variables can be computed in the isentropic framework via the following two steps:

- 1) Estimating the conditional average of thermodynamic state variables as a function of θ_e and z with the formula written as

$$\tilde{f}(\theta_e, z, t) = \frac{\langle \rho f \rangle(\theta_e, z, t)}{\langle \rho \rangle(\theta_e, z, t)}, \quad (4)$$

where f denotes a thermodynamic state variable and the numerator and denominator on the right-hand side are derived from Eq. (2) with $\rho w'$ replaced by ρf and ρ , respectively.

- 2) Interpolating the values of the various state variables \tilde{f} along the trajectories.

²The actual deepest cycle is hard to determine in practice because the atmosphere is a continuum fluid. The cycle with $k = 1$ is used here as a representation of the deepest cycle in Edouard as it is rooted near the surface and nearly reaches 14 km at 1200 UTC 14 September as shown in Fig. 2a.

Through the above manipulations, the mean “air parcel” trajectory in (θ_e, z) space can be viewed as the thermodynamic cycle of the heat engine in Edouard, along which the changes of state variables of a fixed mass of dry air are controlled by the thermodynamic relationship (Pauluis 2011); that is,

$$Tds = dh - \alpha dp - \sum_{w=v,l,i} \mu_w dr_w, \quad (5)$$

where T and p are temperature and pressure, respectively; s , h , and α are the moist entropy,³ enthalpy, and specific volume of per unit mass of dry air, respectively; and μ_v , μ_l , and μ_i and r_v , r_l , and r_i are the Gibbs free energy and mixing ratio of water vapor, liquid water, and ice, respectively. The inclusion of Gibbs free energy terms in Eq. (5) is to take account of the thermodynamic impacts related to the addition and removal of water in different phases in the air parcel, which can induce the heat energy input to and loss from the air parcel (Pauluis 2011). Via integrating Eq. (5) along the thermodynamic cycle, the energy conversion in the heat engine can be determined as

$$\underbrace{\oint T ds}_{W_{\max}} = -\underbrace{\oint \alpha dp}_{W} - \underbrace{\oint \sum_{w=v,l,i} \mu_w dr_w}_{-\Delta g}. \quad (6)$$

In Eq. (6), the term on the left-hand side is the net amount of heat energy gained by an air parcel from its environment including surface energy fluxes, absorption and emission of radiation, turbulent mixing, and frictional dissipation along the thermodynamic cycle. It is equivalent to the work that would be done by a Carnot

³Similar to that in Pauluis (2016), the moist entropy is defined as

$$\begin{aligned} s = (C_{pd} + r_i C_i) \ln \left(\frac{\theta_e}{T_f} \right) &= [C_{pd} + r_i C_i + (r_v + r_l) C_l] \ln \left(\frac{T}{T_f} \right) \\ &\quad - R_d \ln \left(\frac{p_d}{p_0} \right) + (r_v + r_l) \frac{L_{f_0}}{T_f} + r_v \frac{L_v}{T} \\ &\quad - r_v R_v \ln(H), \end{aligned}$$

where T is the temperature, H is the relative humidity, and p_d is partial pressure of dry air; C_{pd} , C_i , and C_l are the specific heat capacities at constant pressure of dry air, ice, and liquid water, respectively; while r_v , r_i , r_l , and $r_T = r_v + r_l + r_i$ are the mixing ratios for water vapor, liquid water, ice, and total water, respectively; $p_0 = 10^5$ hPa and $T_f = 273.15$ K are the reference pressure and freezing temperature for water under atmospheric pressure, respectively; R_d and R_v are the specific gas constants of dry air and water vapor; and L_v and L_{f_0} are the latent heat of vaporization taken at the actual temperature and at the triple point, respectively. The expression of s indicates that the entropy has a similar variation as θ_e .

cycle transporting the same amount of entropy (i.e., W_{\max}). The first term on the right-hand side of Eq. (6) is the work (per unit mass of dry air) that is done in the cycle W , which is usually smaller than W_{\max} because of the Gibbs penalty Δg . In the moist atmosphere with precipitation, water is usually added to the air parcel as unsaturated water vapor at low Gibbs free energy and is removed from the air parcel as liquid or ice with comparatively high Gibbs free energy, which corresponds to a positive value of Δg and a reduction of the ability of the thermodynamic cycle to produce mechanical work (Pauluis 2011; Pauluis and Zhang 2017). Also owing to the water in the air parcel, only part of the mechanical work production in the cycle can be employed to generate kinetic energy to strengthen the winds (while also countering dissipation arising from surface friction and turbulence in the free atmosphere), because lifting water expends mechanical work. For brevity, the work done to lift water as the air parcel moves through the cycle is referred to as W_p while the residual mechanical work production is named W_{KE} , which is directed to strengthen and/or sustain TC vertical and horizontal circulations. These terms can be written as

$$W_p = \oint g r_T dz \quad \text{and} \quad W_{KE} = W - W_p, \quad (7)$$

where g is the gravitational acceleration.

3. Evolution of representative thermodynamic cycles during intensification of Edouard

We focus here on the energy conversion in two representative MAFALDA cycles corresponding to $k = 1$ and $k = 9$ in Eq. (3), which are subjectively employed to represent the deepest and the shallower cycles in Edouard. Figures 3a and 3b, respectively, display the time series of the three terms in Eq. (6), that is, W_{\max} , W , and Δg , in the two cycles during the intensification of Edouard. Comparing to the shallower cycle, the magnitudes and variations of W_{\max} and W are much more pronounced in the deepest cycle, especially after the onset of the near-rapid intensification at about 1200 UTC 14 September, which indicates that the deepest cycle is much more pertinent to Edouard’s intensification. This result indicates that, although the shallow overturning circulations make a great contribution to the vertical mass transport (Fang et al. 2017), they may not be efficient in extracting external heat energy and generating kinetic energy during the storm intensification. Therefore, only the energy cycle associated with the deepest overturning circulation is to be investigated in detail in the following sections with the

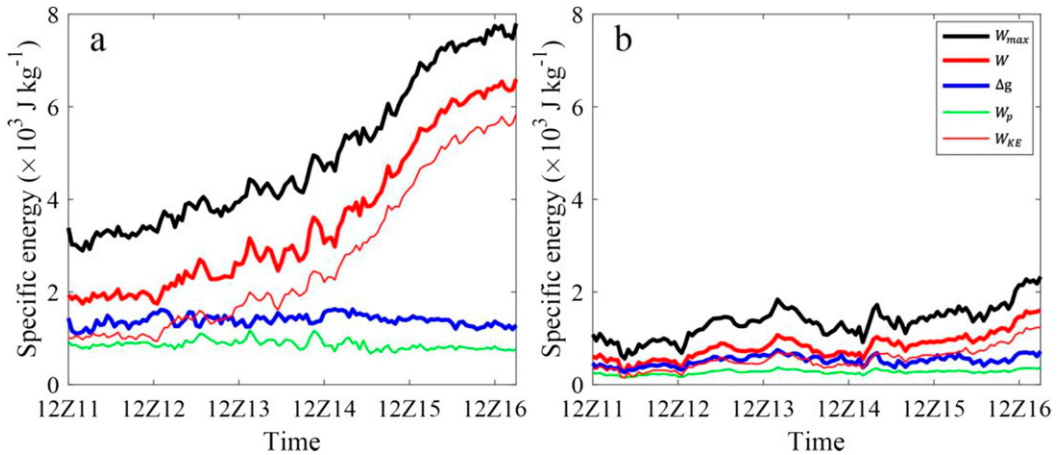


FIG. 3. Time evolution of the work components associated with the (a) deepest and (b) shallower MAFALDA cycles corresponding to the trajectories highlighted by the thick black and thick red curves in Fig. 1a, respectively. The thick black, red, and blue curves denote the maximum work W_{\max} , mechanical work production W , and Gibbs penalty Δg , respectively. The thin red and green curves denote the generation of kinetic energy W_{KE} and work done to lift water W_p , respectively.

aim to understand the intensification of Edouard from the energetics perspective. Figure 3a further shows that the Gibbs penalty Δg (blue line) is smaller than W_{\max} as well as W and does not change noticeably during the intensification of Edouard. Thus, it will not be considered in the following discussion on the energy transfer in the thermodynamic cycle except where noted.

a. MAFALDA cycle for the deepest overturning circulation in the thermodynamic coordinates

TCs intensify via continuously extracting external heat energy from the environment and converting a fraction of it into kinetic energy. From a quantitative point of view, the external heating of per unit mass of dry air δQ is given by

$$\delta Q = Tds + \sum_{w=v,l,i} g_w dr_w = dh - \alpha dp. \quad ^4$$

This “external heating” is the amount of energy gained by a parcel from its “environment” and includes surface energy fluxes, absorption and emission of radiation, turbulent mixing and frictional dissipation. Since the Gibbs free energy is relatively small (Fig. 3a), the external heating is dominated by the change of specific entropy and thus can be readily evaluated through the examination on temperature versus specific entropy diagram, or T – s diagram, for

the thermodynamic cycle. The T – s diagram is a useful and common tool in thermodynamics because it helps to visualize the heat transfer. It has been widely used in the studies on TC intensification from the viewpoint of energy supply (e.g., Tang and Emanuel 2012; Riemer and Laliberté 2015; Gu et al. 2015).

For convenience, we partition the intensification of Edouard into four consecutive stages according to the variation of the minimum sea level pressure: spinup (1200 UTC 11 September–1200 UTC 12 September; stage I), slow intensification (1200 UTC 12 September–1200 UTC 13 September; stage II), fast intensification (1200 UTC 13 September–1200 UTC 14 September; stage III), and near-rapid intensification (1200 UTC 14 September–1200 UTC 16 September; stage IV) of Edouard [refer to Fang et al. (2017) on the stage descriptions]. The respective intensification rates are approximately 3.5, 4.5, 10, and 26 hPa (24 h)⁻¹ in the four stages. The T – s diagrams for the MAFALDA-derived cycles in the four stages are displayed in Fig. 4 with the time interval of 3 h. For convenience, we employ “A,” “B,” “C,” and “D” to respectively denote the point of the lowest entropy (A) and the point of maximum entropy (B) in the near-surface inflow leg, the point of the lowest temperature (C), and the point with the lowest entropy (D) in the whole thermodynamic cycle. In this sense, the MAFALDA cycle is composed of near-surface inflow leg (AB), ascending leg (BC), and descending legs CD and DA, which is similar to the cycle in an idealized hurricane as shown in Pauluis and Zhang (2017).

Figure 4 indicates that the air parcel gains energy as a result of turbulent mixing when it is away from the surface (leg DA) or directly from surface heating (leg

⁴ The addition and removal of water substance in the air parcel can induce variations in the enthalpy of the air parcel and thus can appear as a small energy source (Pauluis 2011; Pauluis and Zhang 2017).

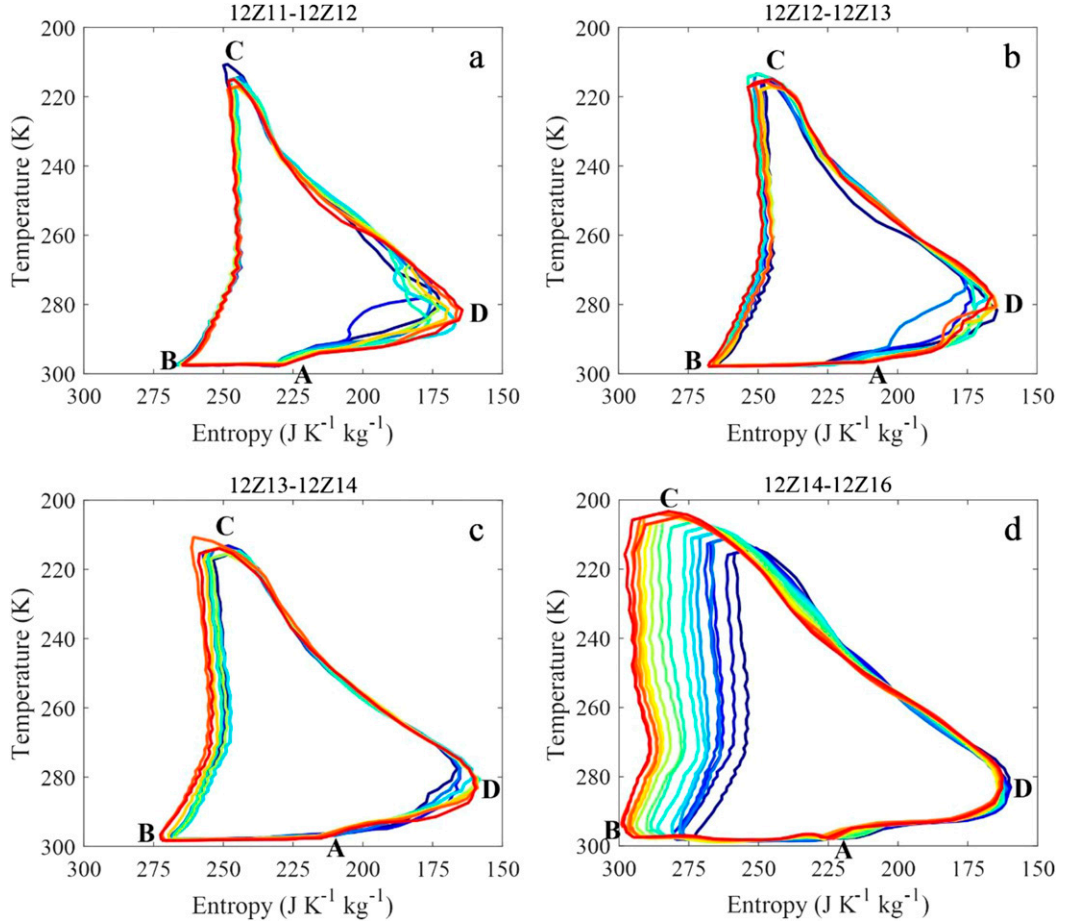


FIG. 4. The T - s diagram for the MAFALDA cycle during the period from (a) 1200 UTC 11 Sep to 1200 UTC 12 Sep, (b) 1200 UTC 12 Sep to 1200 UTC 13 Sep, (c) 1200 UTC 13 Sep to 1200 UTC 14 Sep, and (d) 1200 UTC 14 Sep to 1200 UTC 16 Sep with an interval of 3 h. The trajectories are denoted by the contours with different colors in each period. The cold and warm colors represent the cycles at earlier and later times, respectively. Of note, the axes are reversed (decreasing values away from the origin) here.

AB) when it moves from D to B, while the parcel loses energy, first, mainly through detrainment and mixing during its ascent (leg BC), then by radiation (leg CD) as it moves from B to D. Altogether, energy gained at warmer temperatures is larger than is lost at colder temperatures, a clear signature that the circulation acts as a heat engine (Fig. 3a). Thus, although the MAFALDA cycles shown in Fig. 4 do not completely fit as a classical Carnot heat engine, mostly because the loss of energy is not isothermal and the compression is far from adiabatic, the parcel's trajectory in the T - s coordinates corresponds to a thermodynamic heat engine, with the air parcel gaining energy at a warm temperature and losing it at a colder temperature. Because the air parcel temperature in the MAFALDA cycle is derived from the isentropic-mean temperature at the corresponding altitude, its variation on the lower-temperature side of the descending leg indicates that the

upper-level outflow is vertically stratified in Edouard. This conforms with the TC intensification theory revised by Emanuel and Rotunno (2011) and Emanuel (2012), in which the upper-level outflow temperature is not constant. It is worth noting that the heating reconstructed through MAFALDA is only for a statistically steady system. For the intensifying Edouard, heating recovered by MAFALDA may include the “apparent” heating resulting from changes in the mass distribution (Pauluis and Mrowiec 2013). However, our calculation indicates that, during the intensification of Edouard, the local change of the mass is much smaller than the vertical divergence of vertical mass fluxes in the mass conservation equation in θ_e - z coordinates (figure not shown). Therefore, the apparent heating due to the transient behavior of Edouard should only account for a small fraction of the heating derived from the MAFALDA cycle and thus will not be discussed further hereafter.

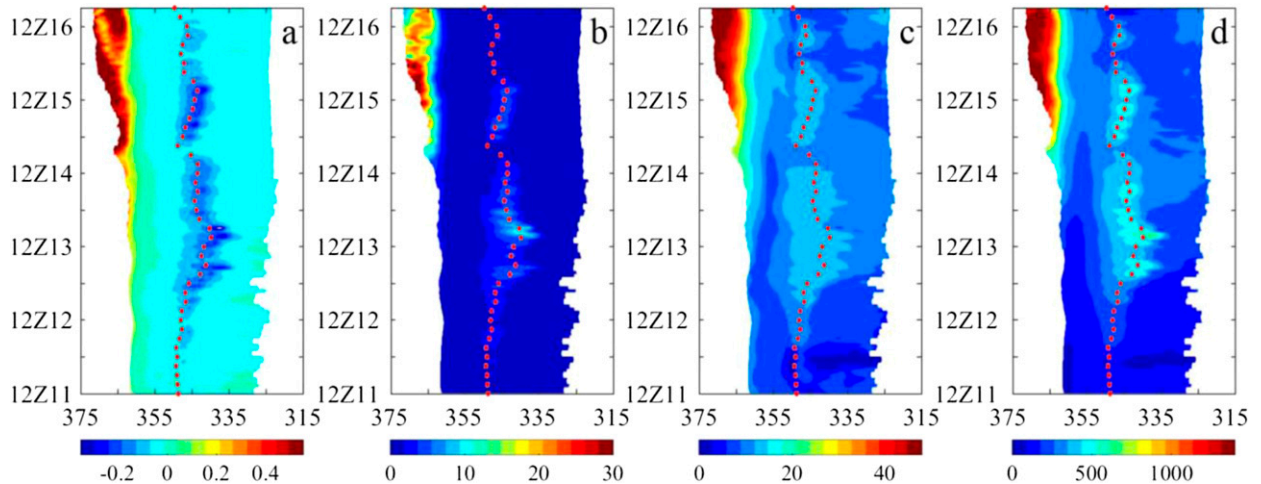


FIG. 5. (a) Time evolution of the mean low-level vertical velocity (m s^{-1}) in the air column with the air parcel that is moving along leg DA and leg AB. The abscissa axis is equivalent potential temperature (K) with the values decreasing away from the origin. The left and right edges of the shaded area and the red dotted line respectively denote the time changes of the average vertical velocity in the low levels of the air column with the air parcel that is located at points B, D, and A. The intervals between the consecutive red dots are 3 h. (b)–(d) As in (a), but for the hourly rain rate (mm h^{-1}), 10-m wind speed (m s^{-1}), and sea surface heat flux (summation of sensible and latent heat fluxes; W m^{-2}), respectively.

During the heating legs (DA and AB), air parcels are injected in the mixed layer and gradually gain energy from the surface exchange. To better elucidate this heating process, we turn to Fig. 5. The isentropic-mean variables shown in Fig. 5 are functions of θ_e of the air parcel that is moving from D through A to B,⁵

⁵ The variables shown in Fig. 5 are determined in the similar way as that in the calculation of the thermodynamic variables along the MAFALDA cycle described in section 2. Taking the sea surface heat flux as an example, the calculation is performed via the following steps. First, the values of density weighted surface heat flux (ρF) are sorted according to the equivalent potential temperature at different altitudes; that is,

$$\langle \rho F \rangle(\theta_{e_0}, z, t) = \iint_A \rho F(x, y) \delta\{\theta_{e_0} - \theta_e(x, y, z, t)\} dx dy.$$

Second, the conditional average of F as function of θ_e and z is estimated with the formula written as

$$\tilde{F}(\theta_e, z, t) = \frac{\langle \rho F \rangle(\theta_e, z, t)}{\langle \rho \rangle(\theta_e, z, t)},$$

where $\tilde{F}(\theta_e, z, t)$ denotes the isentropic-mean surface heat flux under the air parcel locating at (θ_e, z) . Via interpolating the values of \tilde{F} along leg DA and leg AB in the MAFALDA cycle, the isentropic-mean surface heat flux under the air parcel locating at leg DA and leg AB can be finally estimated, which is shown in Fig. 5d. By replacing F in the above formulas with the mean vertical velocity averaged between $z = 1$ and 2 km, hourly rain rate, and 10-m wind speed, the isentropic-mean low-level vertical velocity, hourly rain rate, and 10-m wind speed in the air column with the air parcel that is moving along leg DA and leg AB can also be determined and are shown in Figs. 5a, 5b, and 5c, respectively.

depicting the near-surface and low-level environment of the air parcel as it moves along leg DA and leg AB. The red dotted line and the left and right edges of the shaded area denote the time variations of θ_e of the air parcels located at points A, B, and D in the cycle, respectively. Because the entropy has the similar variation trend as θ_e (footnote 3), the red dotted line also reflects the time variations of the parcels' entropy when it reaches point A. The isentropic-mean vertical velocity shown in Fig. 5a represents the low-level vertical motion in the air column with the air parcel that is moving along leg DB (DA + AB). From Fig. 5a, we can see that, as the air parcel moves along leg DB, the air column it passed through is dominated by weak subsidence in the lower troposphere. However, there are two noticeable exceptions. One is the air parcels on the high θ_e side rise, with the low-level vertical velocity up to 0.4 m s^{-1} corresponding to the air parcels in the eyewall. Another is the region of strong downward velocity, with the low-level vertical velocity of -0.2 m s^{-1} for the values of θ_e between 335 and 355 K . This strong descent corresponds to the mesoscale downdraft associated with the outer rainband, as indicated in Fig. 5b. Interestingly, the point A, which corresponds to the location where the reconstructed cycle makes contact with the surface, can be found in the middle of the region of strong downward motion. This indicates a potentially substantial role of the mesoscale downdraft in pushing down the inflow into the mixed layer. The mesoscale downdraft also corresponds to an enhanced surface winds (Fig. 5c) and surface heat flux (summation of sensible and latent heat fluxes; Fig. 5d).

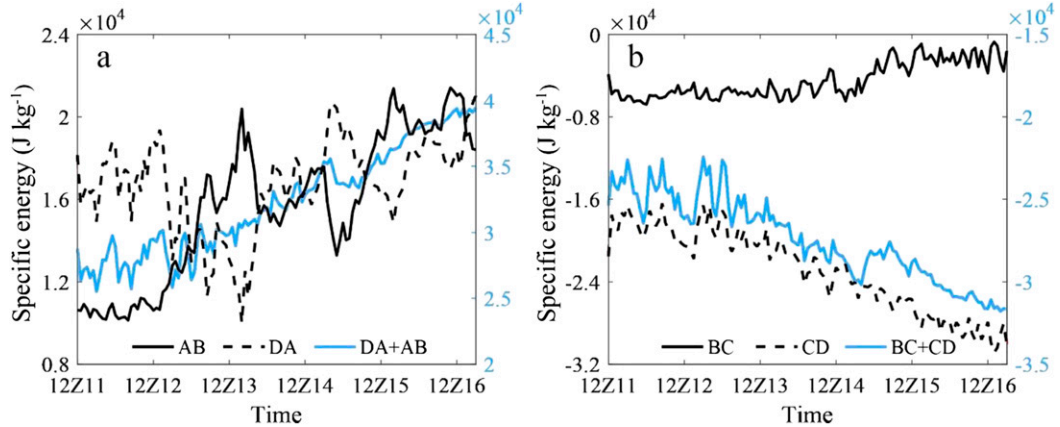


FIG. 6. Time evolution of the integral of Tds (a) from A to B (black solid) and from D to A (black dashed) as well as (b) from B to C (black solid) and from C to D in the MAFALDA cycle during the intensification of Edouard. The blue curves in (a) and (b) denote the integral of Tds from D to B through A and from B to D through C, respectively.

In stage I (Fig. 4a), the MAFALDA cycle in $s-T$ space does not show significant changes except at D, the point with the lowest entropy, which wobbles slightly likely because of the changes in the large-scale environment of Edouard. Accordingly, the external heating responsible for the entropy changes in legs AB and BC (i.e., $\int_{AB} T ds$ and $\int_{BC} T ds$) is nearly constant while its counterpart in legs DA and CD (i.e., $\int_{DA} T ds$ and $\int_{CD} T ds$) fluctuates gently (Figs. 6a,b). Over the entire cycle, W_{\max} is positive in stage I (Fig. 3a), which means that the air parcel gains more energy from the external heating than it loses to the external cooling, with the imbalance compensating for the mechanical work production and Gibbs penalty. Figure 6a further reveals that $\int_{DA} T ds$ is much larger than $\int_{AB} T ds$ in stage I. This indicates that the air parcel gains more energy as a result of turbulent mixing in the atmosphere than that directly from surface heating in the early development of Edouard. It is also worth noting that the energy loss in the ascending leg (BC) mainly occurs in the lower to midtroposphere (Fig. 4a), which results from the diffusive loss of water vapor due to the entrainment of dry air in the updrafts (Pauluis 2016; Pauluis and Zhang 2017).

During the slow intensification stage (stage II), the point D fluctuates in the $s-T$ space while A shifts toward a lower entropy instead of being nearly constant in entropy as that in stage I (Fig. 4b). The decrease of entropy at A is related to the enhanced subsidence in the low levels of the air column with leg DA going through (Fig. 5a). The subsidence acts to transport (lower) θ_e from the midtroposphere to the lower troposphere and dries the subcloud layer, which suppresses the water collection of the air parcel as it descends from D to the surface, and accordingly leads to a decreased entropy when it reaches point A (Fig. 4b).

and Fig. 5a). In addition, the outward expansion of the secondary circulation and the northwestward movement of Edouard into a drier environment (not shown) also contribute to the entropy decrease at point A in stage II. As a contrast, the point B only oscillates slightly in the $T-s$ diagram during stage II (Fig. 4b), which implies that the air parcel gains more heat energy in leg AB in stage II than stage I to enhance its entropy from the lower value at A to the almost unchanged value at B. Such a heat energy demand is met by the persistent enhancement of the surface heat flux under leg AB in stage II (Fig. 5d). Figure 6a shows that the increase of $\int_{AB} T ds$ overcompensates the decrease of $\int_{DA} T ds$, and thus, the total external heating increases in legs DA and AB in stage II. However, because of the enhanced heat energy loss in leg CD (Fig. 6b), the maximum work W_{\max} only increases slightly in stage II (Fig. 3a). The ascent leg (BC) does not make a notable contribution to the change of W_{\max} during stage II (Fig. 6b).

In stage III (Fig. 4c), the MAFALDA cycle demonstrates a noticeable expansion in $s-T$ space via the decrease of moist entropy at D and the shift of the ascending leg toward higher entropy corresponding to the steady growth of W_{\max} (Fig. 3a). Figure 6 quantitatively shows that the increase of W_{\max} is induced by the strengthening of heat energy transfer in legs DA and AB. There is a rapid growth of external heating occurring mainly in leg DA from about 1600 UTC 13 September to 0400 UTC 14 September and in leg AB from around 0400 to 1200 UTC 14 September. The former is largely due to the weakening of the subsidence in the lower troposphere in the region with air parcels going through leg DA (on the low- θ_e side in Fig. 5a), under which the drying effect of the downdrafts counteracting the impact of the surface

moisture flux is weakened and the environment suppression on the water collection of the air parcel is reduced accordingly. With reference to Figs. 5c and 5d, we can see that the latter is consistent with the strengthening of surface wind speed and surface heat flux under leg AB, especially under the eyewall.

As Edouard starts to intensify rapidly in stage IV, the ascending branch of the MAFALDA cycle shifts steadily toward higher entropy while also deepening and thus reaching substantially lower temperature in the s - T coordinates (Fig. 4d). The steady increase of maximum entropy in the cycle (at point B) is supported by the enhanced surface heat flux resulting from the remarkably strengthened near-surface winds beneath the eyewall (Figs. 5c,d). The area enclosed by the cycle equals the integral $\oint T ds$, and thus, the cycle variations exhibited in Fig. 4d correspond to a significant increase of W_{\max} (Fig. 3a). Quantitatively, such an increase of W_{\max} is ascribed not only to the reinforced heat energy transfer in leg DA or leg AB (Fig. 6a), but also to the decrease of the heat energy loss in leg BC (Fig. 6b). As Edouard intensifies, convection becomes active in the eyewall, which in turn humidifies the troposphere in the inner-core area. Consequently, the entrainment of dry air weakens in the updrafts while the diffusive loss of water vapor decreases as the air parcel moves upward from point B, which leads to the decrease of heat energy loss in the ascending branch and favors the enhancement of W_{\max} .

Figure 6a shows that the external heating in leg DA and leg AB are on opposite ends of a seesaw during stages III and IV. When the former reaches the minimum, the latter is usually at a maximum. Comparing Fig. 5 to Fig. 6a, we can see that the variations of $\int_{\text{DA}} T ds$ and $\int_{\text{AB}} T ds$ are tied to the oscillation of θ_e at A with the interval of about 16 to 24 h in that the maxima (minima) $\int_{\text{AB}} T ds$ ($\int_{\text{DA}} T ds$) mainly occurs when or immediately after θ_e is a minimum at A. Figures 5a and 5b indicate that the variation of θ_e at A is correlated with the precipitation and low-level subsidence in the region with leg DA going through (on the low- θ_e side of A in Figs. 5a,b) in that the enhanced (suppressed) precipitation and low-level subsidence on the low- θ_e side of A usually precede the arrival of θ_e to a minimum (maximum) at A. The near-periodical characteristics in the MAFALDA cycle could be associated with the convective activity as described by Dunion et al. (2014); that is, convection regularly bursts outside of the eyewall and propagates radially outward from the storm with the period of ~ 24 h in a mature TC, and/or is related to the outer spiral rainbands reinitiated quasi periodically under the effect of boundary layer charge–discharge mechanism as discussed in Li and Wang (2012).

b. MAFALDA cycle for the deepest overturning circulation in p - α coordinates

The difference between the energy gain and loss in the MAFALDA cycle equals the amount of internal energy that is converted into mechanical energy. The processes related to such a conversion can be further quantified via examining the MAFALDA cycle in p - α coordinates. To illustrate the variations of the mechanical work along the thermodynamic cycle, the specific volume and pressure of the air parcel are decomposed into two parts;⁶ that is,

$$\alpha = \bar{\alpha} + \alpha' \quad \text{and} \quad p = \bar{p} + p',$$

where $\bar{\alpha}$ and \bar{p} are the mean specific volume and pressure horizontally averaged over the $600 \text{ km} \times 600 \text{ km}$ domain centered at Edouard's center at the initial time (1200 UTC 11 September), while α' and p' denote the deviations of α and p from $\bar{\alpha}$ and \bar{p} , respectively. For convenience, the variables with bars and primes are referred to as mean state and perturbation, respectively. The mechanical work production along the MAFALDA cycle ($-\oint \alpha dp$) is consequently decomposed into four components; that is,

$$-\oint \alpha dp = -\oint \bar{\alpha} d\bar{p} - \oint \alpha d\bar{p} - \oint \bar{\alpha} dp' - \oint \alpha' dp'. \quad (8)$$

The first term on the right-hand side of Eq. (8) corresponds to the change in geopotential energy along the parcel trajectory and cancels out when computed on a cycle. The second integral on the right-hand side of Eq. (8), $-\oint \alpha' d\bar{p}$, can be rewritten as $\oint g[(\alpha - \bar{\alpha})/\bar{\alpha}] dz$ after assuming that the mean pressure field is hydrostatic. This corresponds to the integral of the buoyancy along the cycle. As warm air rises near the warm center of the storm, the contribution from this term is positive, and corresponds to a net generation of kinetic energy. As shown in Fig. 7, the integral $-\oint \alpha' d\bar{p}$ increases as the storm intensifies. Figures 8a–d display the MAFALDA cycle in the α' - \bar{p} coordinates and confirms that the increase in the integral $-\oint \alpha' d\bar{p}$ is induced by the reduction in the density during the ascending leg (BC), especially in the upper troposphere: warmer and lighter air rises to a higher level, which enhances the rate at which kinetic energy is generated.

⁶Because of the large span of pressure values and small variation of specific volume, the change of the MAFALDA cycle in the p - α space is not as evident (not shown) as that in the s - T space during the intensification of Edouard, which requires the decomposition here.

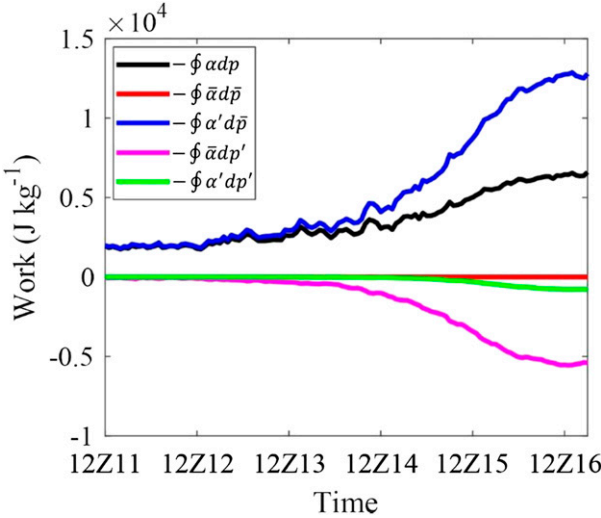


FIG. 7. Time evolution of $-\int \alpha dp$ (black), $-\int \bar{\alpha} d\bar{p}$ (red), $-\int \alpha' d\bar{p}$ (blue), $-\int \bar{\alpha} dp'$ (magenta), and $-\int \alpha' dp'$ (green) in the MAFALDA cycle.

The third term on the right-hand side of Eq. (8) ($-\int \bar{\alpha} dp'$) is negative, but is insufficient to cancel out the generation of kinetic energy arising from the buoyancy contribution [i.e., the second term on the right-hand side of Eq. (8)]. The $\bar{\alpha} - p'$ diagrams for the MAFALDA cycle presented in Figs. 8e–h indicate that the integral $-\int \bar{\alpha} dp'$ arises from two main contributions: 1) a positive contribution due to the horizontal expansion associated with the near-surface

inflow (leg AB) and 2) a negative contribution during the ascending leg BC. During the leg AB, the parcel is near the surface, and moves from the outer region to the storm toward its low pressure center. The substantial drop in the pressure perturbation p' in the center area corresponds to the work done necessary to accelerate the parcel while also balancing the surface friction. In the ascending leg BC, the parcel moves from the center of the storm, where the pressure perturbation is strongly negative, to the upper atmosphere, where the pressure perturbation is much smaller. But because the drop in the pressure perturbation during the leg AB occurs near the surface at lower value of the specific volume while the increase in pressure perturbation in leg BC is accompanied with the increase of the specific volume, the contribution of the later dominates and the integral $-\int \bar{\alpha} dp'$ is negative, reducing the overall generation of kinetic energy. The last term in Eq. (8) is a quadratic term and remains small through the storm intensification.

Comparing Figs. 8a–d to Figs. 8e and 8f, we can see that the total work done during the air parcel in the vertical legs ($\int_{BCDA} -\alpha dp$) is determined by both $-\alpha' d\bar{p}$ and $-\bar{\alpha} dp'$. In the early developing stages (I and II), the work production in the vertical legs is dominated by $\int_{BCDA} -\alpha' d\bar{p}$ and does not exhibit noticeable variations except for magnitude fluctuations (Figs. 8a,b and 8e,f; Fig. 9). After stage II, $\int_{BCDA} -\alpha' d\bar{p}$ begins to increase owing to the volume expansion of the air parcel in the ascending leg (Fig. 8c) while $\int_{BCDA} -\bar{\alpha} dp'$

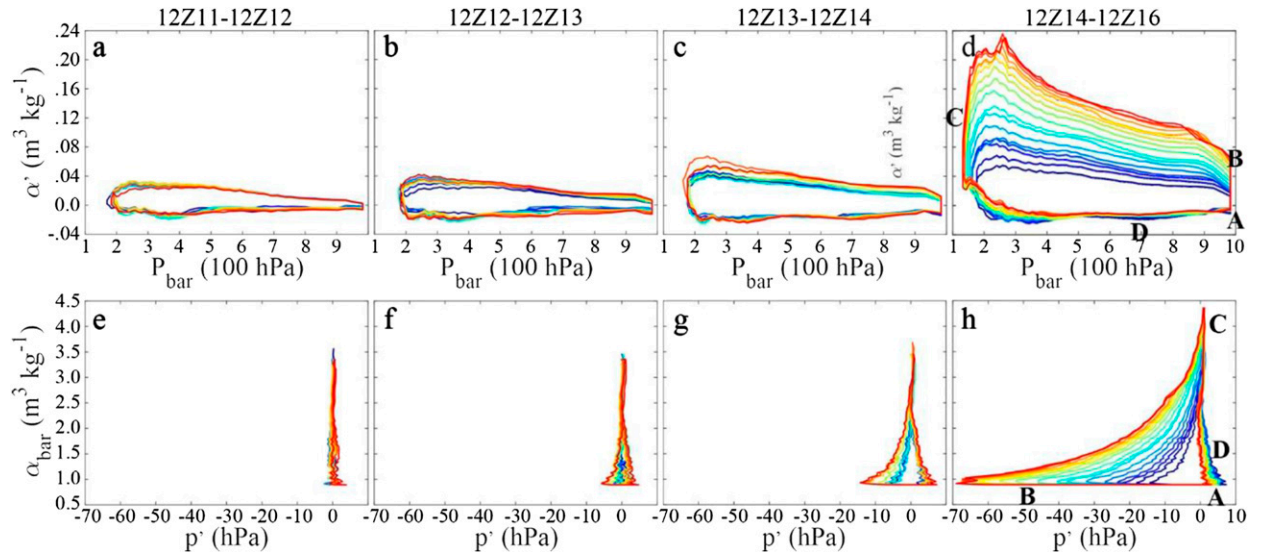


FIG. 8. (a)–(d) The \bar{p} - α' diagram and (e)–(h) the p' - $\bar{\alpha}$ diagram for the MAFALDA cycle during the period from (a),(e) 1200 UTC 11 Sep to 1200 UTC 12 Sep, (b),(f) 1200 UTC 12 Sep to 1200 UTC 13 Sep, (c),(g) 1200 UTC 13 Sep to 1200 UTC 14 Sep, and (d),(h) 1200 UTC 14 Sep to 1200 UTC 16 Sep with a time interval of 3 h. The cycles are denoted by the contours with different colors in each period. The cold and warm colors represent the cycles at early and late times, respectively.

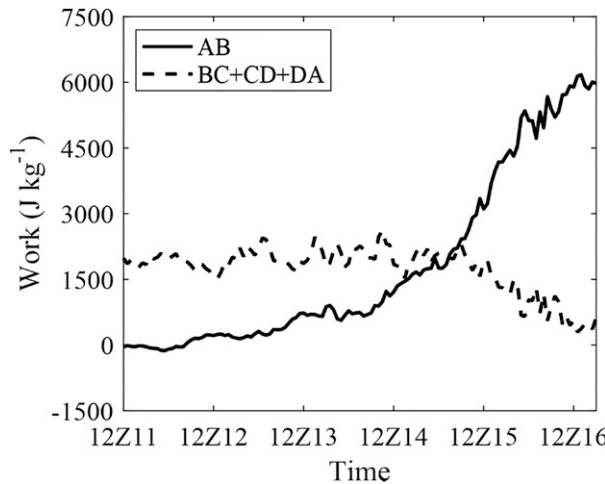


FIG. 9. Time evolution of integral of $-\alpha dp$ from A to B ($\int_{AB} -\alpha dp$; solid line) as well as from B to A through C and D ($\int_{BCDA} -\alpha dp$; dashed line) in the MAFALDA cycle during the intensification of Edouard.

decreases because of the drop of pressure beneath the ascending leg (Fig. 8g). However, the total mechanical work done in the vertical legs does not change considerably in stage III (Fig. 9). As the near-rapid intensification commences, the negative work production term $\int_{BCDA} -\bar{\alpha} dp'$ enhances so fast that its increment becomes larger than the increase in the positive work production term $\int_{BCDA} -\alpha' d\bar{p}$, resulting in slight decrease of the total mechanical work production in the vertical legs of the MAFALDA cycle (Fig. 9). Figure 8 (especially Figs. 8d and 8e) further indicates that mechanical work done during the leg AB is essentially ascribed to the positive contribution due to the horizontal perturbation pressure gradient. It is the work done as the air parcel moves from the outer region to the storm center area with substantial drop in the pressure that dominates the remarkable increase of the mechanical work production W during the intensification of Edouard (Figs. 3a and 9).

From Fig. 9 we also can see that, during the early developing stages (I and II), the mechanical work production in the MAFALDA cycle ($-\oint \alpha dp$) is mainly ascribed to the vertical motion in the ascending and descending legs, which causes the vertical acceleration in the updrafts under the effect of rising warm air. As the storm becomes intense (stages III and IV), the persistent decrease of pressure beneath the eyewall induces a remarkable increase in the work production in the inflow leg, which is mostly utilized to strengthen and/or sustain the horizontal flow. At the same time, the decrease of the pressure beneath the eyewall also reduces the work production in the vertical legs. As a result, the work done in the cycle becomes more and more directed at

intensifying and/or sustaining horizontal winds rather than providing vertical acceleration for the updrafts.

c. Efficiency of the thermodynamic cycle as Edouard intensifies

Because of the water vapor, raindrops, and ice coexisting with dry air in an air parcel, only part of the mechanical work production W_{KE} can be utilized to generate kinetic energy, and the other part W_p is consumed by lifting water as the air parcel moves along the MAFALDA cycle. Figure 3a shows that W_p is nearly constant during the intensification of Edouard. It is somewhat larger than W_{KE} in stage I and then becomes much smaller than W_{KE} , indicating that more and more mechanical work production is employed to generate kinetic energy to accelerate the parcel while also countering dissipation arising from the frictional effect (rather than lifting water) as Edouard intensifies.

In energetics, how much of the external heat energy of a heat engine obtained can be converted to the kinetic energy represents the efficiency of the heat engine. Taking the dynamic and thermodynamic influences of water substance in the air parcel into account, the actual efficiency of the heat engine depicted by the MAFALDA cycle in Fig. 2a can be written as

$$\eta = \frac{W_{KE}}{Q_{in}}, \quad (9)$$

where Q_{in} is the summation of positive values of $T \delta s + \sum_{w=v,l,i} g_w \delta r_w$ in the cycle. According to Eq. (9) in Pauluis and Zhang (2017), the relationship between the actual efficiency and the well-known Carnot efficiency [$\eta_C = (T_{in} - T_{out})/T_{in}$, where T_{in} and T_{out} are the temperatures of the energy source and sink] can be rewritten as

$$\eta = \eta_C - \frac{W_p}{Q_{in}} - \frac{\Delta G}{Q_{in}}, \quad (10)$$

where ΔG is associated with the Gibbs penalty.⁷ Equation (10) shows that the actual efficiency is lower than η_C as it is reduced because of the impacts of inefficiencies in the system. For a moist atmosphere, the two main inefficiencies arise from diffusion of water vapor and from the frictional dissipation induced by falling rainfall (Pauluis and Held 2002a,b). Since the Gibbs energy is fairly small during the intensification of Edouard (Fig. 3a), Q_{in} can be approximated by $\int_{DA+AB} T ds$.

⁷The expressions of ΔG , as well as T_{in} and T_{out} , can be found in Pauluis and Zhang (2017).

Figure 6a manifests that Q_{in} increases as Edouard intensifies. In contrast, the work done to lifting water and the Gibbs penalty do not vary notably during the intensification (Fig. 3a). Therefore, the most significant deviation of actual efficiency from the Carnot efficiency happens in stage I when Q_{in} is small (Fig. 6a and Fig. 10). After stage I, the differences between the actual efficiency and the Carnot efficiency decreases along with the increase of Q_{in} . At around 1200 UTC 16 September, the actual and Carnot efficiencies are about 12.6% and 16.5%, respectively. The difference between the efficiencies is smaller than that in stage I. The prominent increases of the actual and Carnot efficiencies in stage IV indicate that the heat engine is more efficient in an intense TC vortex.

According to Eqs. (7) and (9), the actual efficiency can also be expressed as

$$\eta = \frac{\int_{AB} -\alpha dp}{Q_{\text{in}}} + \frac{\int_{BCDA} -\alpha dp - W_p}{Q_{\text{in}}}. \quad (11)$$

The first term on the right-hand side corresponds to the efficiency referred to as η_{AB} associated with the conversion of internal energy into kinetic energy during the horizontal expansion (leg AB), while the second term corresponds to the remainder associated with the vertical overturning and the work done to lifting water. As indicated by Figs. 9 and 10, the intensification of Edouard is associated with an overall increase that is primarily due to the increase in the expansion working the inflow. In the early development of Edouard, most of the work production can be attributed to the vertical overturning and the combination of warm air rising and cold air subsidence [i.e., the second term on the right-hand side of Eq. (11)]. However, as the storm intensifies, the increase in horizontal pressure gradient allows for an increase in the contribution from the horizontal expansion. In fact, by the end of the simulation, the total efficiency can be approximated by the contribution from the horizontal expansion alone.

4. Concluding remarks

Our study offers a thermodynamic analysis of the energetics during the intensification of Hurricane Edouard (2014). We apply an isentropic framework to sort the flow properties in terms of equivalent potential temperature and height. In doing so, one can compute an overturning mass transport characterized by the ascent of warm moist air at high θ_e and the subsidence of colder and drier air at low θ_e and capture the thermodynamic characteristic of

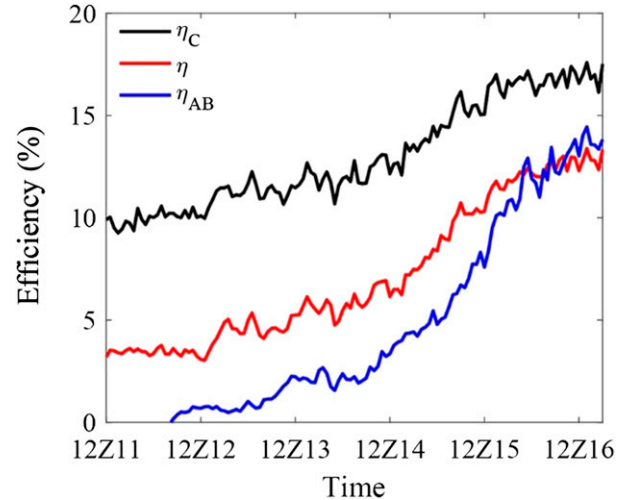


FIG. 10. Time evolution of Carnot efficiency η_C (black), actual efficiency η (red), and the ratio of mechanical work production in leg AB to the total heat energy source η_{AB} (blue) during the intensification of Edouard.

the air motions associated with the upward energy transport. Mrowiec et al. (2016) have shown that the isentropic mass transport is substantially stronger than the secondary (or Eulerian) circulation, as the latter omits the overturning associated with convective motions and thus accounts only for a fraction of the energy transport. In addition, by averaging the flow at constant value of θ_e , one can take advantage of the conservation properties of the equivalent potential temperature so that the mean flow in isentropic coordinates is more closely related to the actual parcel trajectories.

We also apply the Mean Airflow as Lagrangian Dynamics Approximation (MAFALDA) proposed by Pauluis (2016) to extract the thermodynamic cycles associated with Edouard. The reconstructed thermodynamic cycles in Edouard exhibit the characteristics of a heat engine: air parcels acquire energy at high temperature near Earth's surface and lose energy in the upper atmosphere at lower temperature. This differential heating makes it possible for the overturning circulation to generate kinetic energy, albeit the amount of kinetic energy that is generated is strongly affected by the hydrological cycle.

This method allows us to directly relate the energy transport to the energy transport in a thermodynamically consistent manner. In particular, MAFALDA uses the correct expression for the Gibbs relationship for an open system, including the contribution of the Gibbs free energy of water, which has been systematically neglected in the literature [see Pauluis (2011) for a discussion]. Previous studies have shown that the Gibbs penalty substantially reduces the work done by a

moist atmosphere when compared to an equivalent Carnot cycle (Pauluis and Held 2002a,b; Pauluis 2011; Laliberté et al. 2015; Pauluis 2016). Our analysis here confirm a key finding of Pauluis and Zhang (2017) that the Gibbs penalty is substantially less severe for the deepest circulation than it is for moist convection in general.

When a thermodynamic cycle is presented in the entropy-temperature (s - T) coordinates, the maximum work that could be performed by a heat engine is equal to the area within the cycle. In the context of our analysis, the intensification of Edouard appears as a gradual expansion of the thermodynamic cycle in s - T coordinates after the early developing stages (I and II), first as a slight expansion of the thermodynamic cycle toward the low entropy side (stage III), then as a remarkable extension of the cycle toward the high entropy side while also deepening and thus reaching substantially lower temperature (stage IV). The expansion toward high value of entropy is supported by the strengthening of surface heat fluxes in the inner-core region resulting from the strong near-surface winds. The most significant increase of the maximum work happens in the near-rapid intensification stage. During this stage, the low-level dry air entrainment weakens in the inner-core region, which also facilitates the increase of the maximum work.

While the surface entropy maximum increases substantially during the intensification, the minimum entropy of the air parcel in the near-surface inflow leg actually fluctuates on a time scale of about 16–24 h when Edouard is intense (stages III and IV), which is attributable to the reinforcement of the mesoscale downdrafts linked with the near-periodical precipitation in the outer region of the storm. The subsidence transports low- θ_e air from the midtroposphere to the lower troposphere and dries the subcloud layer. The drier environment suppresses the water collection of the air parcel as it descends to the surface.

The increase of the maximum work during the intensification is directly tied to an increase in the generation of kinetic energy in the storm. In the early development of Edouard, vertical expansion dominates the production of mechanical work. As the storm intensifies, the surface pressure decreases continuously in the eye and eyewall, and an increasing fraction of the work production occurs during the horizontal expansion of the air parcel near the surface. The dominant role of the near-surface inflow leg in mechanical work production indicates that, as Edouard intensifies, the mechanical work done in the cycle directs more and more toward strengthening and/or sustaining the horizontal winds rather than providing a vertical acceleration of the updrafts.

Our analysis complements the findings of Pauluis and Zhang (2017) in that TC (Edouard) is less efficient than the classical Carnot cycle because of the hydrological cycle. However, as Edouard intensifies, the differences between the actual and Carnot efficiencies become smaller. After the fast increase in the near-rapid intensification stage, the actual efficiency reaches its maximum of about 12.6%. The increase of actual efficiency means that the heat engine becomes more efficient when the storm becomes more intense.

The current work manifests that the methodology of MAFALDA introduced by Pauluis (2016) and Pauluis and Zhang (2017) provides a unique perspective on the thermodynamic processes in the intensification of Edouard. It is capable of depicting the essential characteristics of an intensifying TC consistent with the traditional analyses: for example, (i) TC gains more and more energy as it intensifies, (ii) the most significant increase of net heat energy acquisition coincides with the near-rapid intensification onset, and (iii) the outer-core region has quasi-periodic features. More than that, the MAFALDA analysis provides quantitative description on the evolution of the thermodynamic cycles during the TC intensification under the impact of precipitation, sea surface heat flux, and dry air entrainment, which can be employed to quantitatively evaluate the intensification of TCs in different developing stages. It is worthy of mentioning that the results presented in this work are based on the definition that the thermodynamic cycle is the deepest cycle among the 20 trajectories determined according to Eq. (3). The external heating, work production, and efficiency of the heat engine in Edouard may be sensitive to the definition of thermodynamic cycle. However, the results are generally not particularly sensitive to the choice of the thermodynamic cycle for the comparison between the different stages of intensification of a TC.

Acknowledgments. The authors are grateful to helpful and constructive comments by three anonymous reviewers of the manuscript. This work was supported in part by the National Key Research and Development Program of China under Grant 2017YFC1501601, National Natural Science Foundation of China Grants 41875067, U.S. Office of Naval Research Grant N000141812517, and National Science Foundation Grant AGS 1712290. Computing is performed at the Texas Advanced Computing Center and High Performance Computing Center of Nanjing University.

REFERENCES

Anthes, R. A., 1974: The dynamics and energetics of mature tropical cyclones. *Rev. Geophys. Space Phys.*, **12**, 495–522, <https://doi.org/10.1029/RG012i003p00495>.

Charney, J. G., and A. Eliassen, 1964: On the growth of the hurricane depression. *J. Atmos. Sci.*, **21**, 68–75, [https://doi.org/10.1175/1520-0469\(1964\)021<068:OTGOTH>2.0.CO;2](https://doi.org/10.1175/1520-0469(1964)021<068:OTGOTH>2.0.CO;2).

Dunion, J. P., C. D. Thorncroft, and C. S. Velden, 2014: The tropical cyclone diurnal cycle of mature hurricanes. *Mon. Wea. Rev.*, **142**, 3900–3919, <https://doi.org/10.1175/MWR-D-13-00191.1>.

Eliassen, A., and E. Kleinschmidt, 1957: Dynamic meteorology. *Handbuch der Physik*, Vol. 48, Springer, 64–72.

Emanuel, K. A., 1986: An air-sea interaction theory for tropical cyclones. Part I: Steady-state maintenance. *J. Atmos. Sci.*, **43**, 585–604, [https://doi.org/10.1175/1520-0469\(1986\)043<0585:AASITF>2.0.CO;2](https://doi.org/10.1175/1520-0469(1986)043<0585:AASITF>2.0.CO;2).

—, 2012: Self-stratification of tropical cyclone outflow. Part II: Implications for storm intensification. *J. Atmos. Sci.*, **69**, 988–996, <https://doi.org/10.1175/JAS-D-11-0177.1>.

—, and R. Rotunno, 2011: Self-stratification of tropical cyclone outflow. Part I: Implications for storm structure. *J. Atmos. Sci.*, **68**, 2236–2249, <https://doi.org/10.1175/JAS-D-10-05024.1>.

Fang, J., O. Pauluis, and F. Zhang, 2017: Isentropic analysis on the intensification of Hurricane Edouard (2014). *J. Atmos. Sci.*, **74**, 4177–4197, <https://doi.org/10.1175/JAS-D-17-0092.1>.

Gu, J., Z.-M. Tan, and X. Qiu, 2015: Effects of vertical wind shear on inner-core thermodynamic of an idealized simulated tropical cyclone. *J. Atmos. Sci.*, **72**, 511–530, <https://doi.org/10.1175/JAS-D-14-0050.1>.

Laliberté, F., J. Zika, L. Mudryk, P. J. Kushner, J. Kjellsson, and K. Döös, 2015: Constrained work output of the moist atmospheric heat engine in a warming climate. *Science*, **347**, 540–543, <https://doi.org/10.1126/science.1257103>.

Leighton, H., S. Gopalakrishnan, J. A. Zhang, R. F. Rogers, Z. Zhang, and V. Tallapragada, 2018: Azimuthal distribution of deep convection, environmental factors and tropical cyclone rapid intensification: A perspective from HWRF ensemble forecasts of Hurricane Edouard (2014). *J. Atmos. Sci.*, **75**, 275–295, <https://doi.org/10.1175/JAS-D-17-0171.1>.

Li, Q., and Y. Wang, 2012: Formation and quasi-periodic behavior of outer spiral rainbands in a numerically simulated tropical cyclone. *J. Atmos. Sci.*, **69**, 997–1020, <https://doi.org/10.1175/2011JAS3690.1>.

Melhauser, C., F. Zhang, Y. Weng, Y. Jin, H. Jin, and Q. Zhao, 2017: A multiple-model convection-permitting ensemble examination of the probabilistic prediction of tropical cyclones: Hurricanes Sandy (2012) and Edouard (2014). *Wea. Forecasting*, **32**, 665–668, <https://doi.org/10.1175/WAF-D-16-0082.1>.

Mrowiec, A. A., O. M. Pauluis, and F. Zhang, 2016: Isentropic analysis of a simulated hurricane. *J. Atmos. Sci.*, **73**, 1857–1870, <https://doi.org/10.1175/JAS-D-15-0063.1>.

Munsell, E. B., J. A. Sippel, S. A. Braun, Y. Weng, and F. Zhang, 2015: Dynamics and predictability of Hurricane Nadine (2012) evaluated through convection-permitting ensemble analysis and forecasts. *Mon. Wea. Rev.*, **143**, 4514–4532, <https://doi.org/10.1175/MWR-D-14-00358.1>.

—, F. Zhang, J. A. Sippel, S. A. Braun, and Y. Weng, 2017: Dynamics and predictability of the intensification of Hurricane Edouard (2014). *J. Atmos. Sci.*, **74**, 573–595, <https://doi.org/10.1175/JAS-D-16-0018.1>.

—, —, S. A. Braun, J. A. Sippel, and A. C. Didlake, 2018: The inner-core temperature structure of Hurricane Edouard (2014): Observations and ensemble variability. *Mon. Wea. Rev.*, **146**, 135–155, <https://doi.org/10.1175/MWR-D-17-0095.1>.

Ooyama, K., 1964: A dynamical model for the study of tropical cyclone development. *Geofis. Int.*, **4**, 187–198.

Pauluis, O., 2011: Water vapor and mechanical work: A comparison of Carnot and steam cycles. *J. Atmos. Sci.*, **68**, 91–102, <https://doi.org/10.1175/2010JAS3530.1>.

—, 2016: The mean air flow as Lagrangian dynamics approximation and its application to moist convection. *J. Atmos. Sci.*, **73**, 4407–4425, <https://doi.org/10.1175/JAS-D-15-0284.1>.

—, and I. M. Held, 2002a: Entropy budget of an atmosphere in radiative–convective equilibrium. Part I: Maximum work and frictional dissipation. *J. Atmos. Sci.*, **59**, 125–139, [https://doi.org/10.1175/1520-0469\(2002\)059<0125:EBOAAI>2.0.CO;2](https://doi.org/10.1175/1520-0469(2002)059<0125:EBOAAI>2.0.CO;2).

—, and —, 2002b: Entropy budget of an atmosphere in radiative–convective equilibrium. Part II: Latent heat transport and moist processes. *J. Atmos. Sci.*, **59**, 140–149, [https://doi.org/10.1175/1520-0469\(2002\)059<0140:EBOAAI>2.0.CO;2](https://doi.org/10.1175/1520-0469(2002)059<0140:EBOAAI>2.0.CO;2).

—, and A. A. Mrowiec, 2013: Isentropic analysis of convective motions. *J. Atmos. Sci.*, **70**, 3673–3688, <https://doi.org/10.1175/JAS-D-12-0205.1>.

—, and F. Zhang, 2017: Reconstruction of the thermodynamic cycles in a high-resolution simulation of a hurricane. *J. Atmos. Sci.*, **74**, 3367–3381, <https://doi.org/10.1175/JAS-D-16-0353.1>.

Riemer, M., and F. Laliberté, 2015: Secondary circulation of tropical cyclones in vertical wind shear: Lagrangian diagnostic and pathways of environmental interaction. *J. Atmos. Sci.*, **72**, 3517–3536, <https://doi.org/10.1175/JAS-D-14-0350.1>.

Rogers, R. F., J. A. Zhang, J. Zawislak, H. Jiang, G. R. Alvey III, E. J. Zipser, and S. N. Stevenson, 2016: Observations of the structure and evolution of Hurricane Edouard (2014) during intensity change. Part II: Kinematic structure and the distribution of deep convection. *Mon. Wea. Rev.*, **144**, 3355–3376, <https://doi.org/10.1175/MWR-D-16-0017.1>.

Rotunno, R., and K. A. Emanuel, 1987: An air-sea interaction theory for tropical cyclones. Part II: Evolutionary study using a non-hydrostatic axisymmetric numerical model. *J. Atmos. Sci.*, **44**, 542–561, [https://doi.org/10.1175/1520-0469\(1987\)044<0542:AAITFT>2.0.CO;2](https://doi.org/10.1175/1520-0469(1987)044<0542:AAITFT>2.0.CO;2).

Skamarock, W. C., and J. B. Klemp, 2008: A time-split non-hydrostatic atmospheric model for research and NWP applications. *J. Comput. Phys.*, **227**, 3465–3485, <https://doi.org/10.1016/j.jcp.2007.01.037>.

Stewart, S. R., 2014: Tropical cyclone report: Hurricane Edouard (AL062014). NOAA/National Hurricane Center Tech. Rep. AL062014, 19 pp., http://www.nhc.noaa.gov/data/tcr/AL062014_Edouard.pdf.

Tang, B., and K. Emanuel, 2012: Sensitivity of tropical cyclone intensity to ventilation in an axisymmetric model. *J. Atmos. Sci.*, **69**, 2394–2413, <https://doi.org/10.1175/JAS-D-11-0232.1>.

Tang, X., and F. Zhang, 2016: Impacts of the diurnal radiation cycle on the formation, intensity, and structure of Hurricane Edouard (2014). *J. Atmos. Sci.*, **73**, 2871–2892, <https://doi.org/10.1175/JAS-D-15-0283.1>.

—, Z.-M. Tan, J. Fang, Y. Q. Sun, and F. Zhang, 2017: Impact of the diurnal radiation cycle on secondary eyewall formation. *J. Atmos. Sci.*, **74**, 3079–3098, <https://doi.org/10.1175/JAS-D-17-0020.1>.

Weng, Y., and F. Zhang, 2016: Advances in convection-permitting tropical cyclone analysis and prediction through EnKF assimilation of reconnaissance aircraft observations. *J. Meteor. Soc. Japan*, **94**, 345–358, <https://doi.org/10.2151/jmsj.2016-018>.

Zhang, F., and Y. Weng, 2015: Predicting hurricane intensity and associated hazards: A five-year real-time forecast experiment with assimilation of airborne Doppler radar observations. *Bull. Amer. Meteor. Soc.*, **96**, 25–32, <https://doi.org/10.1175/BAMS-D-13-00231.1>.

—, —, J. A. Sippel, Z. Meng, and C. H. Bishop, 2009: Cloud-resolving hurricane initialization and prediction through assimilation of Doppler radar observations with an ensemble Kalman filter: Humberto (2007). *Mon. Wea. Rev.*, **137**, 2105–2125, <https://doi.org/10.1175/2009MWR2645.1>.

—, —, J. F. Gamache, and F. D. Marks, 2011: Performance of convection-permitting hurricane initialization and prediction during 2008–2010 with ensemble data assimilation of inner-core airborne Doppler radar observations. *Geophys. Res. Lett.*, **38**, L15810, <https://doi.org/10.1029/2011GL048469>.